J. Fluid Mech. (2001), *vol.* 431, *pp.* 43–63. Printed in the United Kingdom

Partial cavity flows. Part 2. Cavities forming on test objects with spanwise variation

By K. R. LABERTEAUX AND S. L. CECCIO

Department of Mechanical Engineering and Applied Mechanics, University of Michigan,
Ann Arbor, MI 48109-2121, USA

(Received 12 April 1999 and in revised form 31 August 2000)

Partial cavitation forming on the vertex of a wedge and on the leading edge of a stationary hydrofoil was experimentally examined. The geometry of these test objects varied in the spanwise direction (i.e. three-dimensional test objects). Closed cavities formed on these test objects. The interface of the closed cavities curved smoothly to form a re-entrant jet at the cavity terminus, and the re-entrant flow was directed spanwise, thus preventing its impingement on the cavity interface. The cavity shape and the pressure gradients near the closure of the closed cavities were qualitatively similar to those predicted with the two-dimensional free-streamline theory. These cavities had a steady, laminar flow reattachment. The flow around the closed cavity was largely irrotational.

1. Introduction

Attached or sheet cavitation occurs when a flowing liquid continuously detaches from a solid surface to form a vapour film. The flow in the closure of partial cavities can vary substantially, with *open* cavities shedding small and large vapour filled vortices and *closed* cavities shedding few or no bubbles. As discussed in Laberteaux & Ceccio (2001) (hereafter referred to as Part 1), open cavities result when adverse pressure gradients in the cavity closure region cause substantial condensation of the cavity. If the pressure field near the cavity interface does not lead to condensation, the cavity surface can close back to form a re-entrant cavity closure. This re-entrant flow can lead to the filling and break-off cycle that results in the formation of cloud cavitation. This type of closure resulted in an *unsteady re-entrant* cavity. While all of the cavities examined in Part 1 were open, partial cavities can terminate without the creation of vapour clouds. Such closed cavities are often observed on test objects that have significant variation in their geometry, such as propellers and impellers.

Most laboratory studies of partial cavitation have examined cavitation that formed on two-dimensional hydrofoils (i.e. hydrofoils with a rectangular planform and with a constant section profile and pitch across the span). Fewer fundamental studies have been performed on three-dimensional hydrofoils. Crima (1970), Bark (1985, 1986), and Ihara, Watanabe & Shizukuishi (1989) examined attached cavitation that formed on stationary hydrofoils with significant sweep. De Lange (1996) examined both open and closed cavities that formed on two- and three-dimensional stationary hydrofoils. For a two-dimensional cavity, the cavity closure line was perpendicular to the flow direction. Any re-entrant flow that formed would travel directly upstream toward the cavity detachment point. However, if the cavity flow was three-dimensional, the closure line was often no longer perpendicular to the mean flow direction. The re-entrant flow then entered the cavity at an angle that was not parallel to the mean flow direction. Cavities that formed on three-dimensional test objects were often substantially different in appearance compared to those formed on two-dimensional or axisymmetric test objects. The directed re-entrant flow on three-dimensional test objects was captured numerically by Dang & Kuiper (1999).

In the present study, we extend our study of partial cavities to those that form on test models that vary in the spanwise direction. Spanwise sweep was introduced to the two-dimensional models examined in Part 1. Two objects were examined: a swept wedge and swept plano-convex hydrofoils. *Incipient* cavities were examined on all of the test objects under certain conditions. As partial cavities developed, *closed* cavities were observed. Unlike the *unsteady re-entrant* cavities examined in Part 1, the closed cavities forming on the swept test objects were quite steady. We will use the following definition with regard to these cavities:

> *Steady re-entrant cavity.* The cavity is largely vapour filled, and the cavity interface closes back at the cavity terminus to form a thin re-entrant flow. The flow closes behind the cavity via a laminar reattachment. The re-entrant flow is directed in the spanwise direction and does not locally impinge on the cavity interface. The local cavity geometry is steady.

The flows near the closure region of these cavities were examined in order to reveal the origin of these different developed cavities. In addition, results from the two-dimensional analytical model of closed partial cavities discussed in Part 1 were qualitatively compared with the observed *closed* cavities.

2. Experimental methods

The experiments described here were conducted in the Cavitation and Multiphase Flow Laboratory at the University of Michigan, Department of Mechanical Engineering and Applied Mechanics. Experiments were conducted in the Blow Down Water Tunnel (BDWT), which is described in detail by Tassin, Ceccio & Bernal (1995). The BDWT permits control of both the free-stream velocity and pressure, and free and dissolved gas contents were qualitatively controlled. Small gas bubbles were allowed to rise to a free surface before tests were performed, and the dissolved gas content was approximately 30% of the saturated concentration at atmospheric conditions. Several techniques were employed for qualitative and quantitative flow analysis, including flash photography, particle streak photography (PSP), single-frame particle image velocimetry (PIV), and cinemagraphic PIV. A detailed description of these techniques, along with the experimental apparatus and test procedures, is given in Part 1. Figure 1 shows a typical double-pulsed image and processed PIV image for the flow around the cavity on the swept test object. In this case, the light sheet intersects the cavity near the mid-span. Because the test object is three-dimensional, a portion of the light sheet near the cavity leading edge is blocked by the cavity between the light sheet and the camera.

A swept wedge and swept plano-convex hydrofoils were used as test models. The swept wedge had a vertex angle of $\beta = 26.5^\circ$, a step height of 19 mm, and a sweep angle of $\gamma = 30^\circ$. The wedge was mounted directly onto a custom-made test section window, and no effort was made to control the wall-bounded flow that formed upstream of the wedge. The wedge was constructed of brass that was highly polished and mounted directly onto a test-section window. The three-dimensional, plano-convex hydrofoils

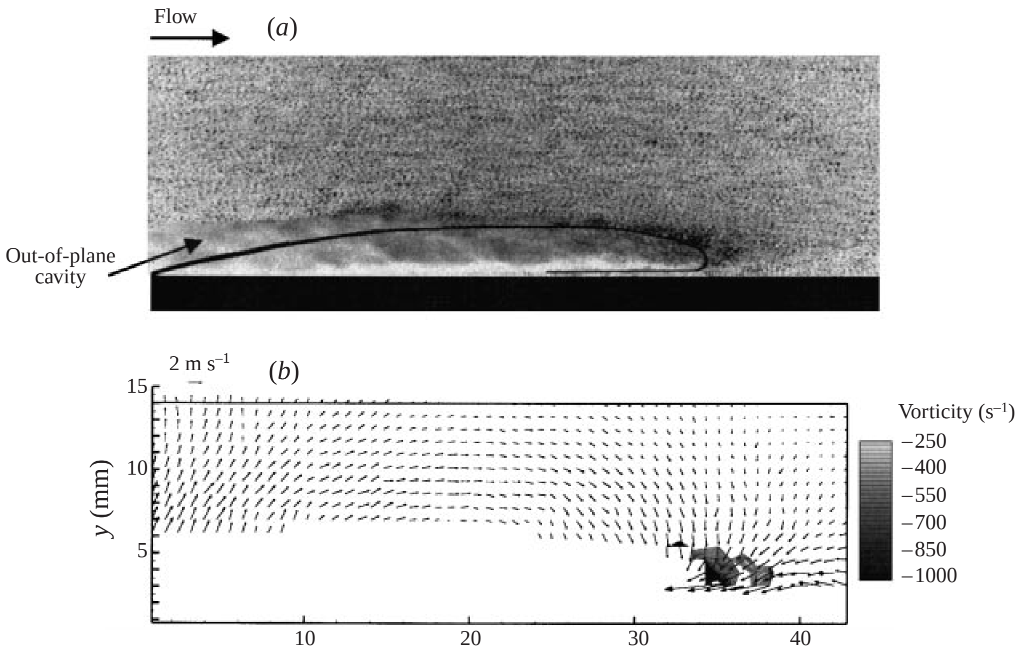

FIGURE 1. (*a*) Double-pulsed PIV image, and (*b*) resulting plot of vorticity. $U = 8.4\,\mathrm{m\,s^{-1}}$, $\sigma = 1.4$. The region indicated above the cavity interface (solid line) is masked by the out-of-plane, three-dimensional cavity.

had sweep angles of 30°, 15°, or 5°. The chord length of the hydrofoils was 127 mm, the width was 78 mm, and the maximum thickness of the hydrofoils was 12.7 mm. The hydrofoils had a round leading edge with radius of 1.6 mm and a flat suction side. This geometry was chosen to achieve separation near the leading edge of the foil. All of the hydrofoils spanned the width of the test section to prevent gap flow at the tip. The hydrofoils were mounted onto an arbour that allowed them to be placed at an attack angle. All hydrofoils were made of brass that was highly polished.

3. Results: partial cavities forming on the three-dimensional objects

The non-cavitating and cavitating flows near the leading edge of the wedge and hydrofoils were examined. For the wedge, the nominal free-stream velocity was $8.5 \pm 0.2\,\mathrm{m\,s^{-1}}$, and the free-stream cavitation number σ was equal to 1.39 ± 0.16. Three swept hydrofoils were examined with sweep angles, γ, of 30°, 15°, and 5°. For the hydrofoils, the angle of incidence of the plano-convex foil, α, was varied from 2° to 5° to achieve a range of cavity geometries. The nominal free-stream velocity was $9.2 \pm 0.5\,\mathrm{m\,s^{-1}}$, making the free-stream Reynolds number based on the hydrofoil chord length, $Re_L = U_\infty L/\nu$, equal to $(1.0 \pm 0.1) \times 10^6$. The three-dimensional cavities were examined at three different spanwise locations on the wedge. Planes parallel to the mean flow direction were examined at locations that were 30%, 50%, and 70% of the line spanning the test section. The location of these planes, shown in figure 2 for the hydrofoil with $\gamma = 30°$, are referred to as the left-, mid-, and right-planes.

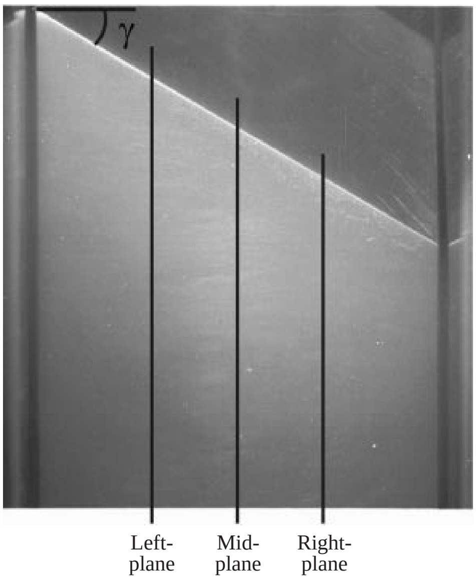

FIGURE 2. Plan view of the location of the three planes used for streak photography. The planes are at 30% (left), 50% (mid), and 70% (right) of the line spanning the test section.

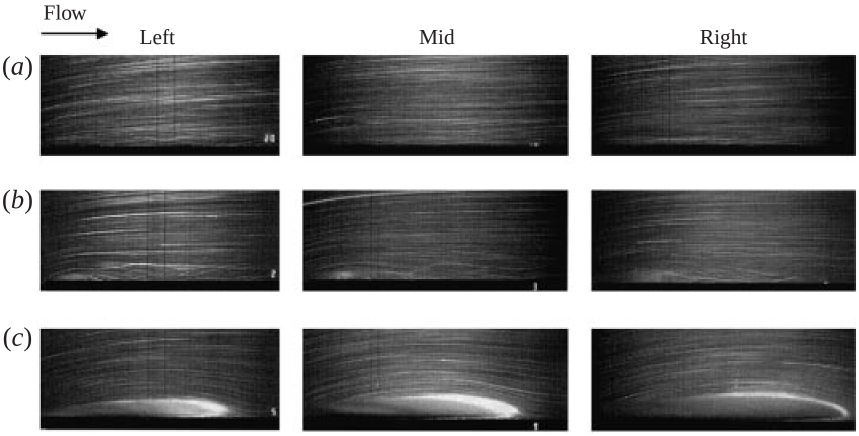

FIGURE 3. Streaks for three planes on the swept wedge $\gamma = 30°$, $\beta = 26.5°$. Left-plane: (*a*) $U = 8.6\,\mathrm{m\,s^{-1}}$, $\sigma = 3.68$ (non-cavitating); (*b*) $U = 8.2\,\mathrm{m\,s^{-1}}$, $\sigma = 1.92$; (*c*) $U = 8.7\,\mathrm{m\,s^{-1}}$, $\sigma = 1.35$. Mid-plane: (*a*) $U = 8.5\,\mathrm{m\,s^{-1}}$, $\sigma = 3.79$; (*b*) $U = 8.2\,\mathrm{m\,s^{-1}}$, $\sigma = 1.90$; (*c*) $U = 8.5\,\mathrm{m\,s^{-1}}$, $\sigma = 1.36$. Right-plane: (*a*) $U = 8.7\,\mathrm{m\,s^{-1}}$, $\sigma = 3.2$; (*b*) $U = 8.3\,\mathrm{m\,s^{-1}}$, $\sigma = 1.88$; (*c*) $U = 8.5\,\mathrm{m\,s^{-1}}$, $\sigma = 1.38$.

3.1. *Non-cavitating flow*

The non-cavitating flow on the swept wedge was examined with particle streak photography (PSP). Figure 3(*a*) illustrates streak photographs on the left-, mid-, and right-planes of the three-dimensional wedge. Similarly to the flow over the two-dimensional wedge discussed in Part 1, the leading-edge flow separated at the vertex of the swept wedge, and the separation bubble had a thickness that was on the same order as the thickness of the boundary layer.

The leading-edge separated region on the three-dimensional plano-convex foils differed from the corresponding separated region on the two-dimensional plano-

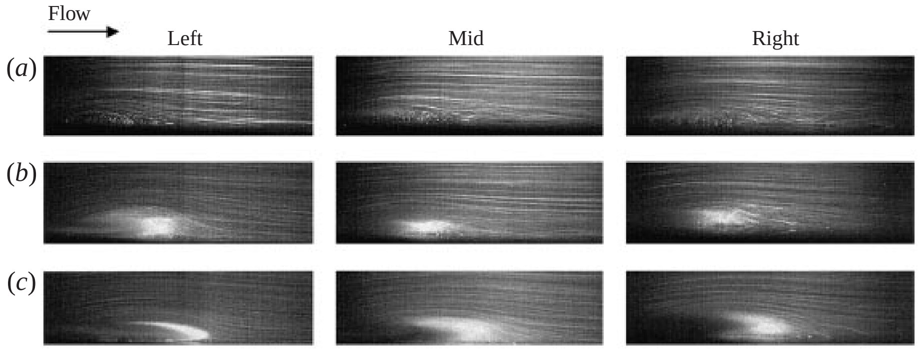

FIGURE 4. Streaks for three planes on the swept hydrofoil $\gamma = 30°$, $\alpha = 2°$. Left-plane: (*a*) $U = 9.1\,\mathrm{m\,s^{-1}}$, $\sigma = 1.3$ (non-cavitating); (*b*) $U = 9.5\,\mathrm{m\,s^{-1}}$, $\sigma = 1.1$; (*c*) $U = 9.6\,\mathrm{m\,s^{-1}}$, $\sigma = 0.9$. Mid-plane: (*a*) $U = 9.2\,\mathrm{m\,s^{-1}}$, $\sigma = 1.3$; (*b*) $U = 9.5\,\mathrm{m\,s^{-1}}$, $\sigma = 1.1$; (*c*) $U = 9.8\,\mathrm{m\,s^{-1}}$, $\sigma = 0.9$. Right-plane: (*a*) $U = 9.2\,\mathrm{m\,s^{-1}}$, $\sigma = 1.3$; (*b*) $U = 9.6\,\mathrm{m\,s^{-1}}$, $\sigma = 1.0$; (*c*) $U = 9.8\,\mathrm{m\,s^{-1}}$, $\sigma = 0.9$. The streamwise extent of the image is approximately 5 cm.

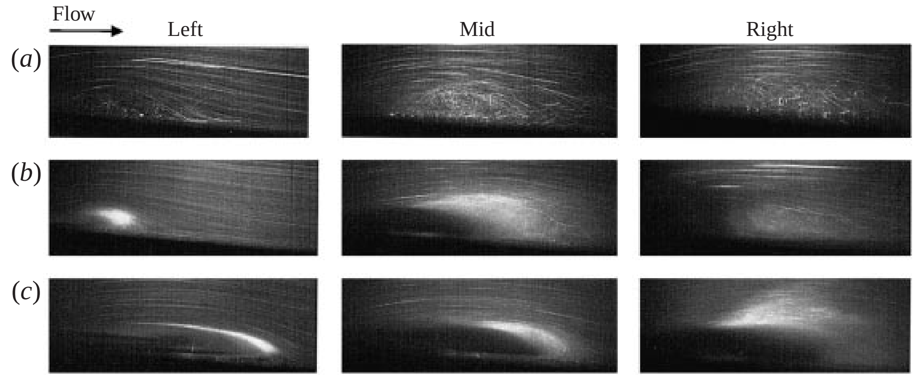

FIGURE 5. Streaks for three planes on the swept hydrofoil $\gamma = 30°$, $\alpha = 5°$. Left-plane: (*a*) $U = 9.0\,\mathrm{m\,s^{-1}}$, $\sigma = 4.5$ (non-cavitating); (*b*) $U = 8.9\,\mathrm{m\,s^{-1}}$, $\sigma = 2.7$; (*c*) $U = 9.6\,\mathrm{m\,s^{-1}}$, $\sigma = 1.7$. Mid-plane: (*a*) $U = 8.7\,\mathrm{m\,s^{-1}}$, $\sigma = 2.85$; (*b*) $U = 9.6\,\mathrm{m\,s^{-1}}$, $\sigma = 1.7$; (*c*) $U = 9.7\,\mathrm{m\,s^{-1}}$, $\sigma = 1.5$. Right-plane: (*a*) $U = 8.9\,\mathrm{m\,s^{-1}}$, $\sigma = 2.5$; (*b*) $U = 9.5\,\mathrm{m\,s^{-1}}$, $\sigma = 1.9$; (*c*) $U = 9.6\,\mathrm{m\,s^{-1}}$, $\sigma = 1.5$. The streamwise extent of the image is approximately 5 cm.

convex hydrofoil discussed in Part 1. The non-cavitating flow on the suction side of the 30° sweep angle hydrofoil is shown in figures 4(*a*) and 5(*a*) for the three planes with the hydrofoil at attack angles of 2° and 5°. The separation bubble grew thicker and longer for planes farther away from the upstream vertex of the hydrofoil, towards the right-plane (70%). On the left-plane (30%), the streamlines near the boundary of the separation bubble reattached smoothly compared with the two-dimensional separation bubble.

Previous experimental observations of highly swept ‘delta’ wings suggest that an attached leading-edge vortex has formed on the swept hydrofoil (see, for example, Thwaites 1960). In this case, there is flow within the separation bubble with a strong component parallel to the direction of the swept leading edge, and the re-entrant flow at the closure of the separation bubble may be entrained into the vortex. Such a process would result in a much smoother flow reattachment compared with the two-dimensional separation bubble. The leading edge vortex will be disturbed at spanwise locations near the right-plane due to the presence of the test section wall.

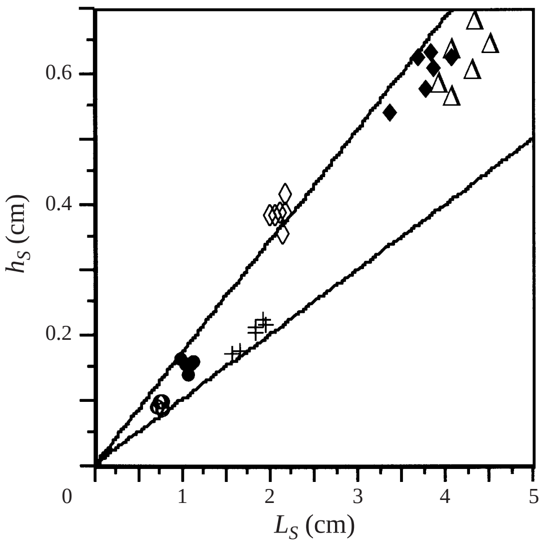

FIGURE 6. Plot of the separation bubble thickness, h_S, versus separation bubble length, L_S, at left-, mid- and right-planes of the three-dimensional hydrofoil, $\gamma = 30°$. $\alpha = 2°$: ○, left-plane; ●, mid-plane; +, right-plane. $\alpha = 5°$: ◇, left-plane; ◆, mid-plane; △, right-plane. The solid lines represent the data for the non-cavitating separation bubble on the two-dimensional hydrofoil (Laberteaux & Ceccio 2001), $h_S/L_S = 0.13 \pm 0.03$.

This is evident from the turbulent reattachment of the separation bubble visualized at the right-plane.

Figure 6 presents a plot of the separation bubble thickness versus the bubble length for $\alpha = 2°$ and 5° for the three spanwise planes. The range, $h_S/L_S = 0.13 \pm 0.03$, determined for the two-dimensional leading-edge separation bubble is also shown. Most of the data fell within this range. At $\alpha = 2°$, the separation bubble on the swept hydrofoil was consistently thicker and longer than the separation bubble observed on the two-dimensional hydrofoil of Part 1. For $\alpha = 5°$, the separation bubble on the swept hydrofoil at the left-plane was much shorter than the equivalent condition on the two-dimensional hydrofoil. $h_S/L_S \approx 0.19$ for this case. Otherwise, the separation bubbles on the mid- and right-planes fell within the data range of the two-dimensional hydrofoil.

3.2. *Cavity inception and appearance*

An attached cavity formed at the vertex of the swept 26.5° wedge as the static pressure in the BDWT test section was lowered. Images of the cavitation are shown in figure 7 for a sweep angle of $\gamma = 30°$, and correspond to three different cavitation numbers. Incipient partial cavitation took place at the upstream vertex of the wedge in the region of flow separation, as seen in figure 7(*a*). A small portion of the separation bubble filled with vapour, while the remaining portion of the separated region exhibited shear layer cavitation. As the cavitation number was reduced, the spanwise extent of the vapour-filled region increased until it spanned the entire test section. A turbulent boundary layer developed on the test section wall, and was ingested into the cavity since the wedge was mounted flush with the test section wall. The ingested turbulent boundary layer was visualized by the wavy appearance of the cavity surface.

The introduction of sweep substantially changed the topology of the partial cavity.

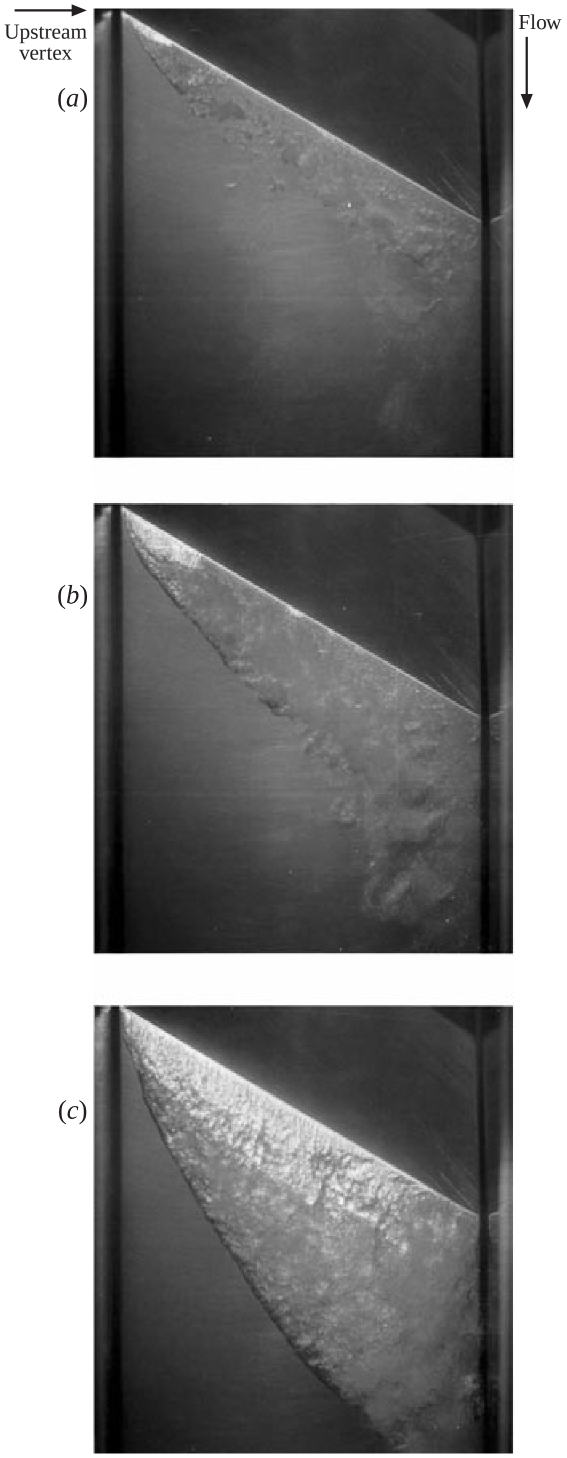

FIGURE 7. Cavitation on the three-dimensional wedge with $\gamma = 30°$, $\beta = 26.5°$. (*a*) $U = 9.4\,\mathrm{m\,s^{-1}}$, $\sigma = 1.81$; (*b*) $U = 9.6\,\mathrm{m\,s^{-1}}$, $\sigma = 1.54$; (*c*) $U = 9.3\,\mathrm{m\,s^{-1}}$, $\sigma = 1.3$. Plan view.

The spanwise variation of the three-dimensional wedge redirected the re-entrant flow, which can be seen through the clear cavity interface. The direction of the flow was approximately perpendicular to the free-stream direction. De Lange (1996) discussed how the re-entrant flow was 'reflected' at the closure of three-dimensional partial cavities, and these observations were consistent with this process. A layer of re-entrant liquid flowed within the cavity until it impinged on the cavity interface near the right test section wall, as seen in figures 7(*b*) and 7(*c*). A liquid/vapour mixture resulted that was similar to that observed on the two-dimensional wedge. This portion of the cavity was open and was associated with the shedding of bubbles and vortical structures. The closure of the vapour-filled cavity was steady, and no bubbles or cavitating vortices were shed downstream. These portions of the cavity were closed.

Figure 3 shows a series of streak images at the three spanwise planes for three different cavitation numbers. Case (*b*) is incipient, and case (*c*) is developed cavitation. Inception started at the upstream vertex of the wedge within the region of flow separation. Initially, the cavitation did not modify the shape of the separation bubble. With decreasing static pressure (cavitation number), the original region of flow separation became completely filled with vapour, and the cavity grew beyond the extent of the original separated region. The closed portion of the cavity spanned the entire test section as the cavitation number was lowered, and became open only as the re-entrant flow interacted with the right test section wall and impinged on the cavity surface. The flow downstream of the cavity at all three planes remained laminar and smoothly reattached to the wedge surface. Large-scale flow separation was not observed in the closure of the cavity.

Similarly, for the swept hydrofoil the free-stream pressure was reduced, and cavitation was observed on the suction side of the hydrofoils. Images of the cavitation are shown in figures 8 and 9 for sweep angles of $\gamma = 30^\circ$, and attack angles of 2° and 5°, respectively. The images shown correspond to three different cavitation numbers. Inception took place at the upstream vertex of the hydrofoil in the region of flow separation, as seen in figures 8(*a*) and 9(*a*). A small portion of the separation bubble filled with vapour, while the remaining portion of the separated region exhibited shear layer cavitation. As the cavitation number was reduced, the spanwise extent of the vapour-filled region increased.

Similar to the three-dimensional wedge, the re-entrant flow can be seen through the smooth cavity interface on the swept hydrofoil. The direction of the flow was approximately perpendicular to the free-stream direction, as seen in figures 8(*b*), 9(*b*), 8(*c*), and 9(*c*). A liquid/vapour mixture resulted that was similar to that observed on the two-dimensional plano-convex hydrofoil. This portion of the cavity was open, and was associated with the shedding of bubbles and vortical structures. In some cases, the vapour-filled cavity reformed after the re-entrant flow had impinged. The closure of the vapour-fllled portion of the cavity was steady, and no bubbles or cavitating vortices were shed downstream. These portions of the cavity were closed. Figure 10 presents a comparison of the partial cavitation that forms on the two-dimensional (Part 1) and the three-dimensional plano-convex hydrofoils for nominally the same test conditions. Introduction of sweep substantially changed the topology of the cavity compared to the cavity forming on the two-dimensional hydrofoil.

Figures 4 and 5 show a series of streak images at the three spanwise planes for three different cavitation numbers and attack angles of 2° and 5°, respectively. Again, case (*b*) is inception, and case (*c*) is developed cavitation. Inception started at the upstream vertex of the hydrofoil within the region of flow separation. The closed

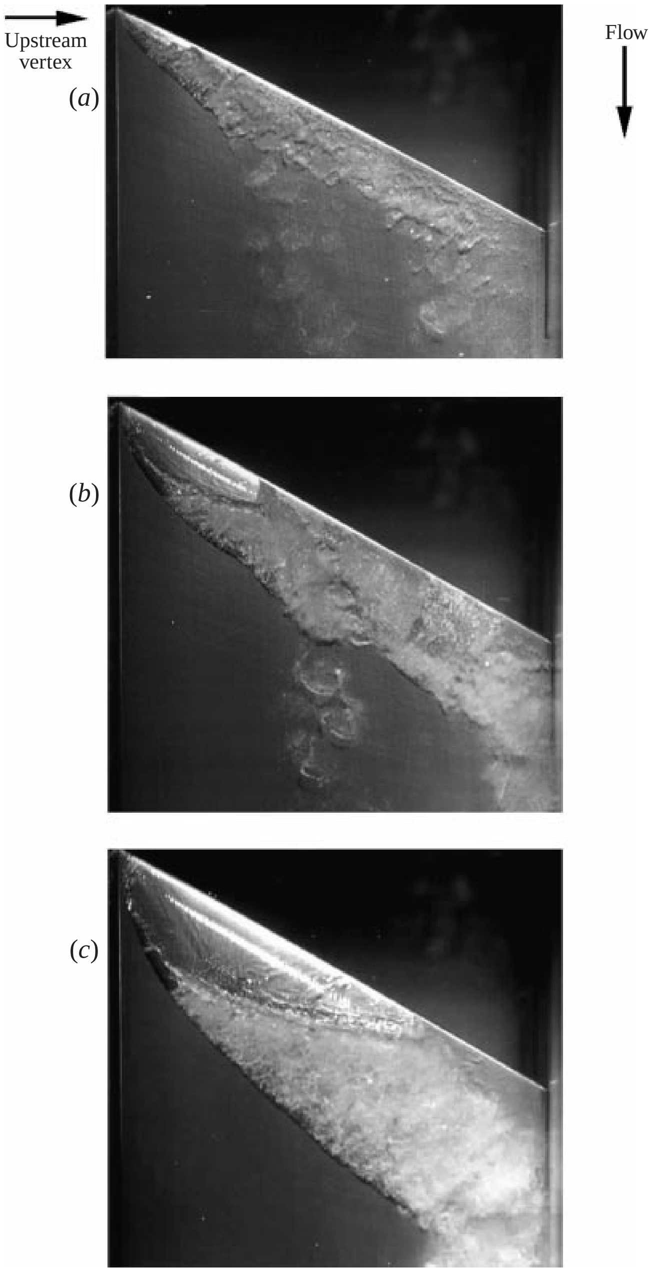

FIGURE 8. Cavitation on the three-dimensional hydrofoil with $\gamma = 30°$, $\alpha = 2°$. (*a*) $U = 9.8\,\mathrm{m\,s^{-1}}$, $\sigma = 1.0$; (*b*) $U = 9.9\,\mathrm{m\,s^{-1}}$, $\sigma = 0.72$; (*c*) $U = 10.1\,\mathrm{m\,s^{-1}}$, $\sigma = 0.7$. Plan view.

portion of the cavity (left-plane) grew beyond the length of the separation bubble as the cavitation number was decreased. The flow downstream of the closed cavity at the left-plane remained laminar. Similar to the three-dimensional wedge, large-scale flow separation was not observed in the closure of the cavity. The cavity at the mid-plane could be either open or closed, depending on the specific condition. The

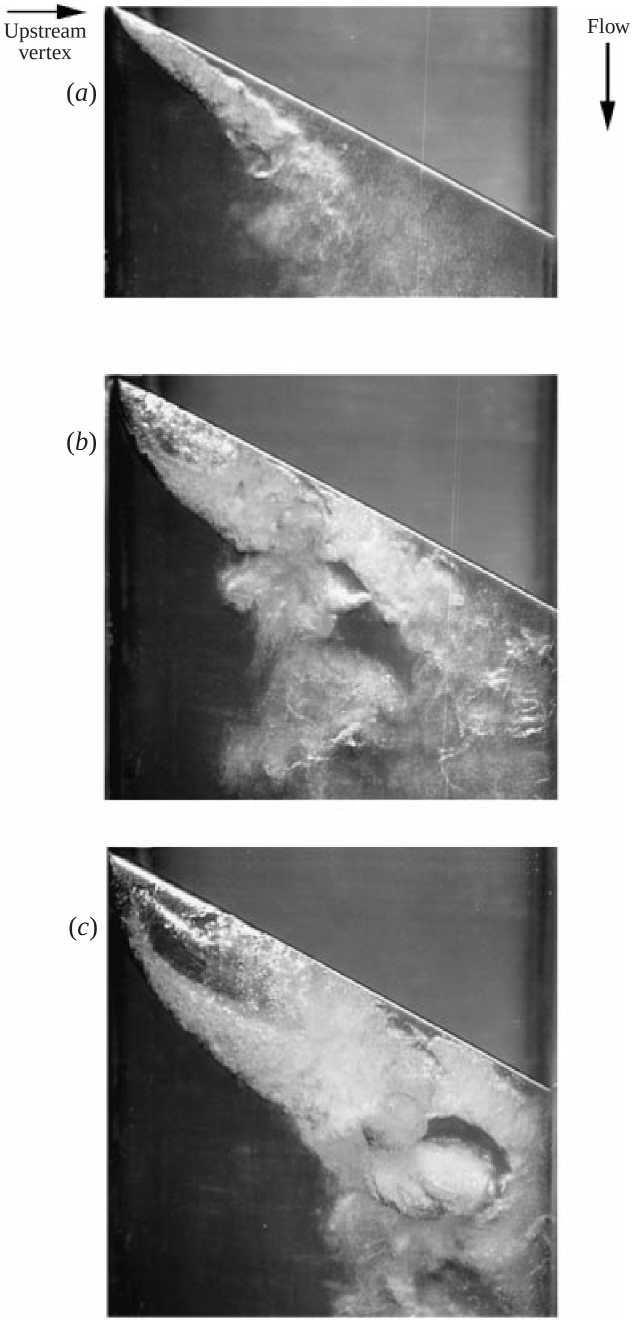

FIGURE 9. Cavitation on the three-dimensional hydrofoil with $\gamma = 30°$, $\alpha = 5°$. (a) $U = 9.0\,\mathrm{m\,s^{-1}}$, $\sigma = 2.4$; (b) $U = 9.6\,\mathrm{m\,s^{-1}}$, $\sigma = 1.9$; (c) $U = 9.6\,\mathrm{m\,s^{-1}}$, $\sigma = 1.5$. Plan view.

open portion of the cavity corresponded with the re-entrant flow impingement on the cavity surface. The cavity at the right-plane was almost always open, but it was possible at low attack angles to have a closed cavity that nearly spanned the test section.

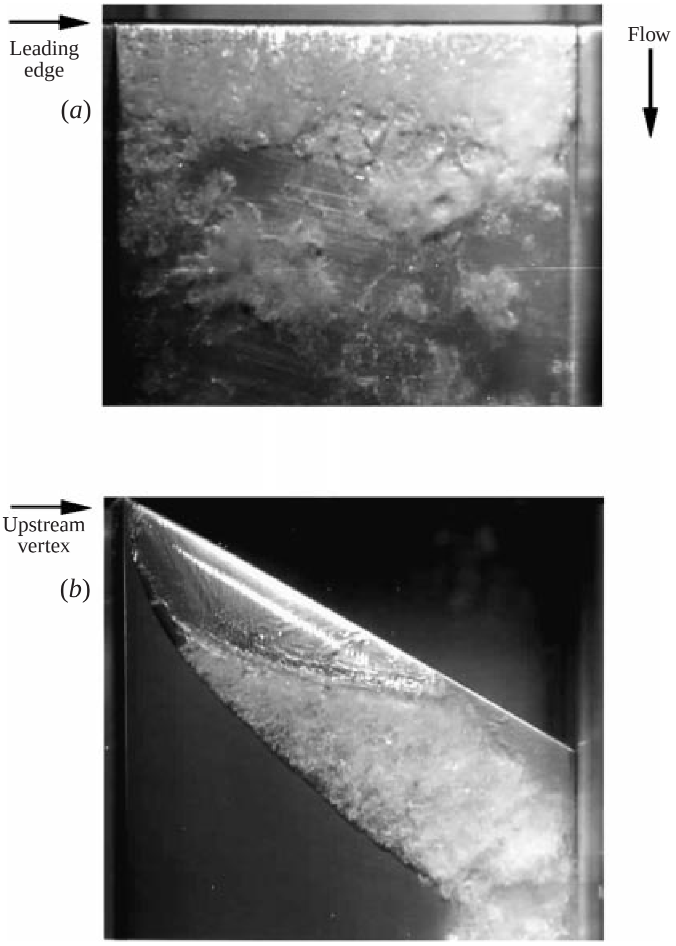

FIGURE 10. (*a*) Two-dimensional plano-convex foil (Laberteaux & Ceccio 2001), $\gamma = 0°$, $\alpha = 2°$, $U = 9.4\,\mathrm{m\,s^{-1}}$, $\sigma = 0.6$. (*b*) Three-dimensional plano-convex foil, $\gamma = 30°$, $\alpha = 2°$, $U = 10.1\,\mathrm{m\,s^{-1}}$, $\sigma = 0.7$. Plan view.

3.3. *Cavity geometry*

Figure 11(*a*) shows the cavity length versus cavity thickness at the three planes of interrogation. $h_C/L_C \approx 0.09$ for the cavities formed on the swept wedge compared to $h_C/L_C \approx 0.14$ for cavities formed on the two-dimensional wedge ($\beta = 26.5°$) (Part 1). Figure 11(*b*) shows the cavity length as a function of cavitation number. The cavitation number necessary to form developed cavitation on the swept wedge was much lower than the value at which similar cavity geometries occurred on the similar two-dimensional wedge (i.e. $\sigma_{2D} = 2.2$ versus $\sigma_{3D} = 1.4$). Moreover, the length of the closed cavity was approximately 1.5–2 times the length of the original non-cavitating separation bubble. It was difficult to measure the cavity geometry for the open portions of the cavities due to the large quantity of shed bubbles and cavitating vortices. Figure 12 presents the cavity maximum thickness versus cavity length for the closed portion of the cavities on the swept hydrofoil.

The cross-sections of the closed portions of the cavity were qualitatively similar to the cavity profiles predicted by free-streamline theory for re-entrant partial cavities

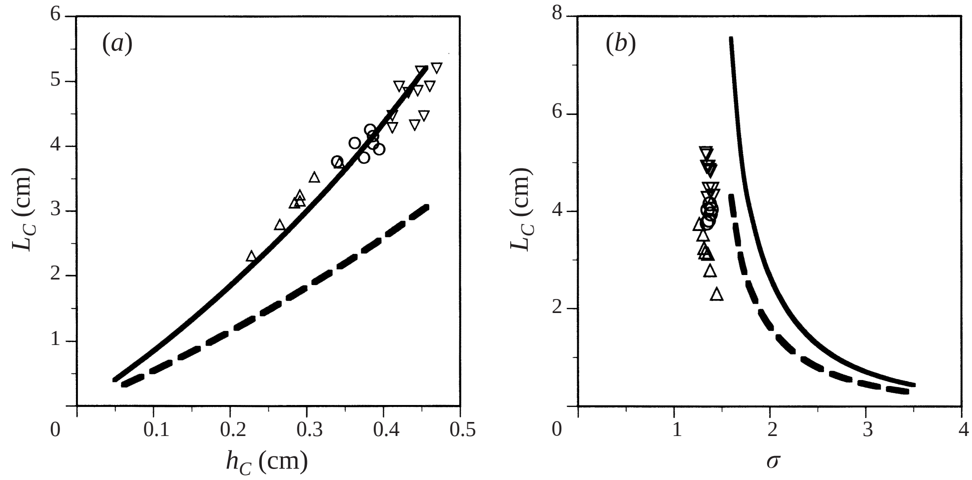

FIGURE 11. Maximum cavity length, L_C, as a function of (*a*) cavity thickness, h_C, and (*b*) cavitation number, σ. Also plotted are the two-dimensional analytical solution for the maximum cavity length (solid line) and the length at the point of maximum thickness (dashed line). Data shown are for the three-dimensional wedge: $\triangle$, left-plane L_C; ○, mid-plane L_C; ∇, right-plane L_C. Uncertainties: $h_C \pm 5\%$, $L_C \pm 5\%$.

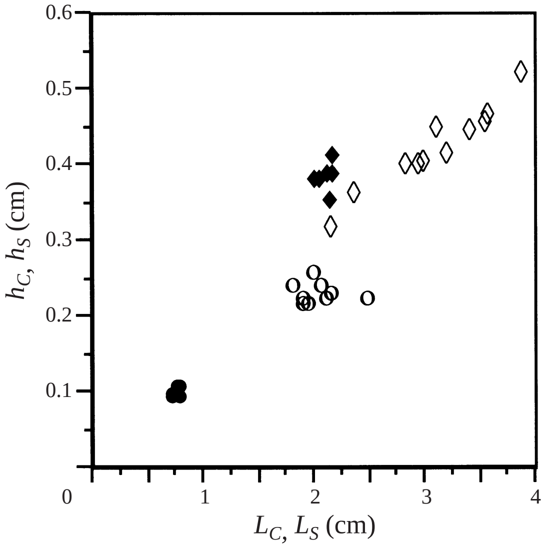

FIGURE 12. Plot of the maximum cavity thickness, h_C, versus cavity length, L_C, for $\alpha = 2°$ (○) and $\alpha = 5°$ (◇), $\gamma = 30°$. Data taken on the left-plane of the three-dimensional hydrofoil for the closed portion of the cavity. Also shown is the non-cavitating separation bubble thickness, h_S, versus separation bubble length, L_S, for $\alpha = 2°$ (●) and $\alpha = 5°$ (◆).

forming on two-dimensional test objects. Such a model for partial cavitation on the two-dimensional wedge was presented in Part 1, and the results of this model can be qualitatively compared to the closed cavities that formed on the swept wedge. The cavity geometry measured for cavities at all three planes on the three-dimensional, swept wedge were similar to the free-streamline theory for two-dimensional cavities. The cavity surface closed back to form a re-entrant jet, and the predicted and

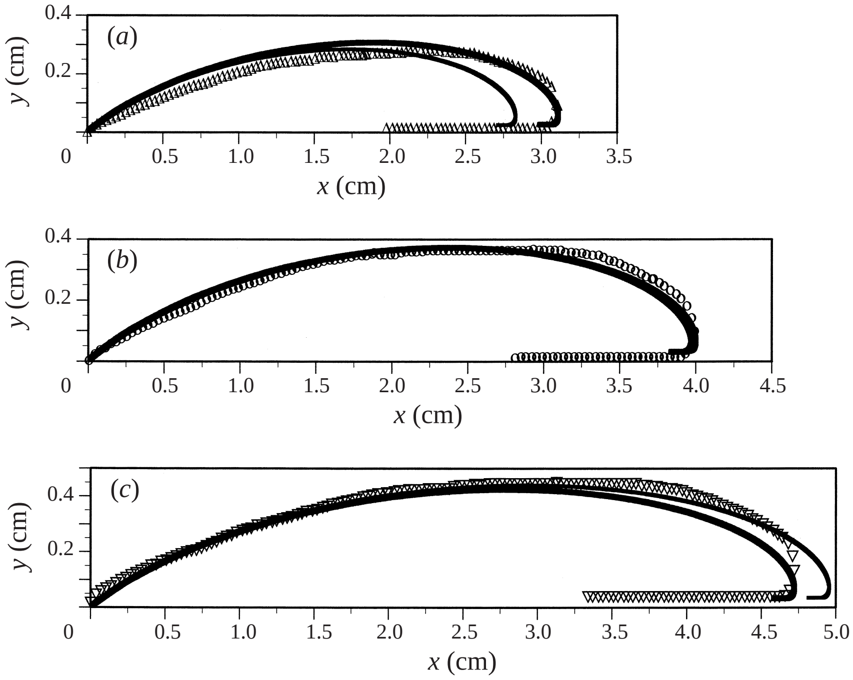

FIGURE 13. Experimentally measured cavity profiles on the three-dimensional wedge, $\beta = 26.5°$, $\gamma = 30°$, and analytically predicted cavity profiles on the two-dimensional wedge (solid lines). Analytical solutions matched to the cavity thickness data and cavity length data are shown. (*a*) Left-plane: $\sigma_{exp} = 1.34$, $\sigma_{anal,h} = 1.97$, $\sigma_{anal,L} = 1.92$. (*b*) Mid-plane: $\sigma_{exp} = 1.36$, $\sigma_{anal,h} = 1.80$, $\sigma_{anal,L} = 1.80$. (*c*) Right-plane: $\sigma_{exp} = 1.36$, $\sigma_{anal,h} = 1.72$, $\sigma_{anal,L} = 1.74$. Uncertainty of σ is $\pm 6\%$.

observed maximum cavity thickness, h_C, versus maximum cavity length, L_C, were comparable. The solid line in figure 11(*a*) represents the maximum predicted length of the two-dimensional cavity, and the dashed line represents the predicted length of the two-dimensional cavity at the point of maximum cavity thickness. For a given cavity thickness, the length was qualitatively predicated. It was not expected that the two-dimensional free-streamline theory would predict the relationship between cavity length and cavitation number since there was one value of σ for the flow, and a range of cavity sectional lengths across the span of the swept wedge. Typical cavity profiles formed on the three planes of the swept wedge are shown in figure 13. Analytical solutions that matched either the measured maximum cavity thickness or length were found, although the analytically determined cavitation number differed at each plane from that of the experimental test condition. The measured values of $h_C/L_C \approx 0.09$ at the left-, mid-, and right-planes indicate that the cavity geometry profile was similar across the span of the three-dimensional wedge. The qualitative characteristics of the cavity were well-predicted on all three planes of interrogation. As the re-entrant flow formed to close the cavity, a laminar stagnation flow formed just downstream of the cavity. The distance from the end of the closed cavity to the stagnation point was found to be $X_{LC} = 0.054 \pm 0.021$ cm for the closed cavity forming at the mid-plane of the swept wedge. This compared to an analytical prediction of $X_{LC} = 0.057$ cm.

A thin re-entrant flow was observed beneath the cavity, and the direction of the flow was approximately in the spanwise direction. This re-entrant flow can be seen in the

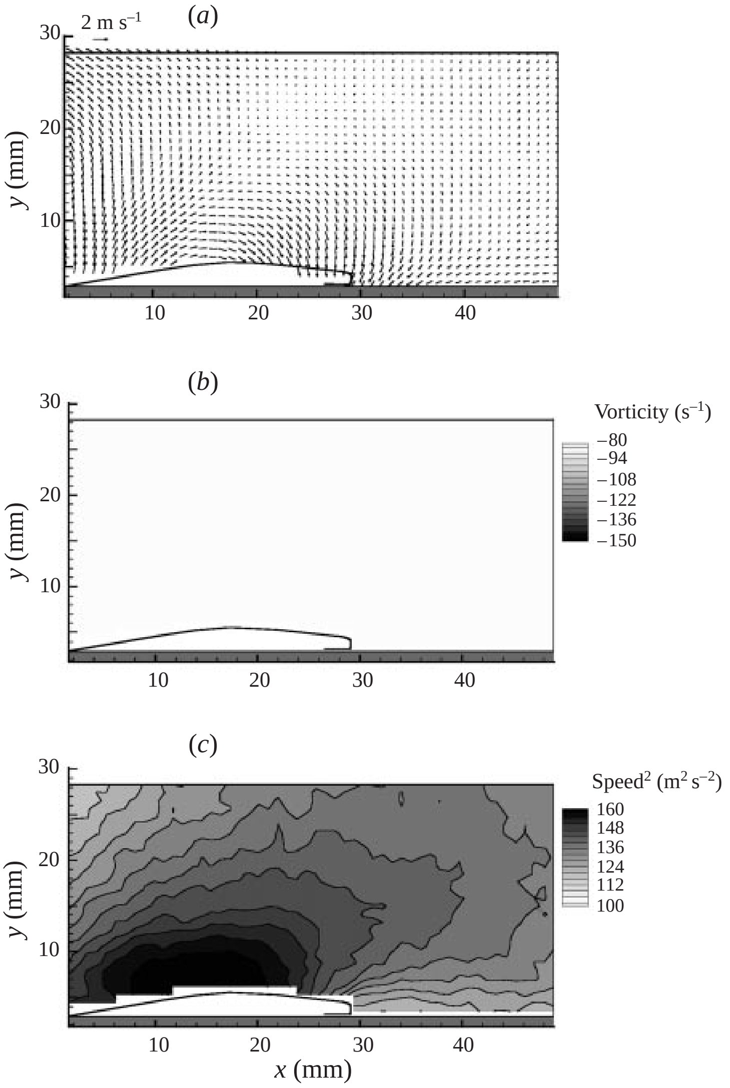

FIGURE 14. Averaged PIV velocity vector field on the three-dimensional wedge, $\beta = 26.5°$, $\gamma = 30°$, $U = 8.4\,\mathrm{m\,s^{-1}}$, $\sigma = 1.5$. (*a*) Velocity field with the global mean subtracted, $U_{gm} = 11.8\,\mathrm{m\,s^{-1}}$, $V_{gm} = 0.7\,\mathrm{m\,s^{-1}}$. (*b*) Vorticity field. (*c*) Flow speed $|\boldsymbol{u}|^2 = u^2 + v^2$. 50 images were processed.

single-shot images of the closed cavity because the clear, vapour-filled cavity allows optical access to the particles entrained in the re-entrant flow. The analytical model of the two-dimensional cavity predicted that the re-entrant flow will be only a few percent of the maximum cavity thickness. The measured jet thickness was similarly thin. A qualitative comparison can be made between the measured jet thickness at the three different planes and the jet thickness of a two-dimensional cavity of similar profile. The predicted re-entrant jet thickness for the three two-dimensional cavities shown in figure 13 were $l_{j,left} = 0.026\,\mathrm{cm}$, $l_{j,mid} = 0.029\,\mathrm{cm}$, and $l_{j,right} = 0.032\,\mathrm{cm}$. The measured jet thickness at all three planes for the cavities on the swept wedge was $l_{j,exp} = 0.03\,\mathrm{cm}$.

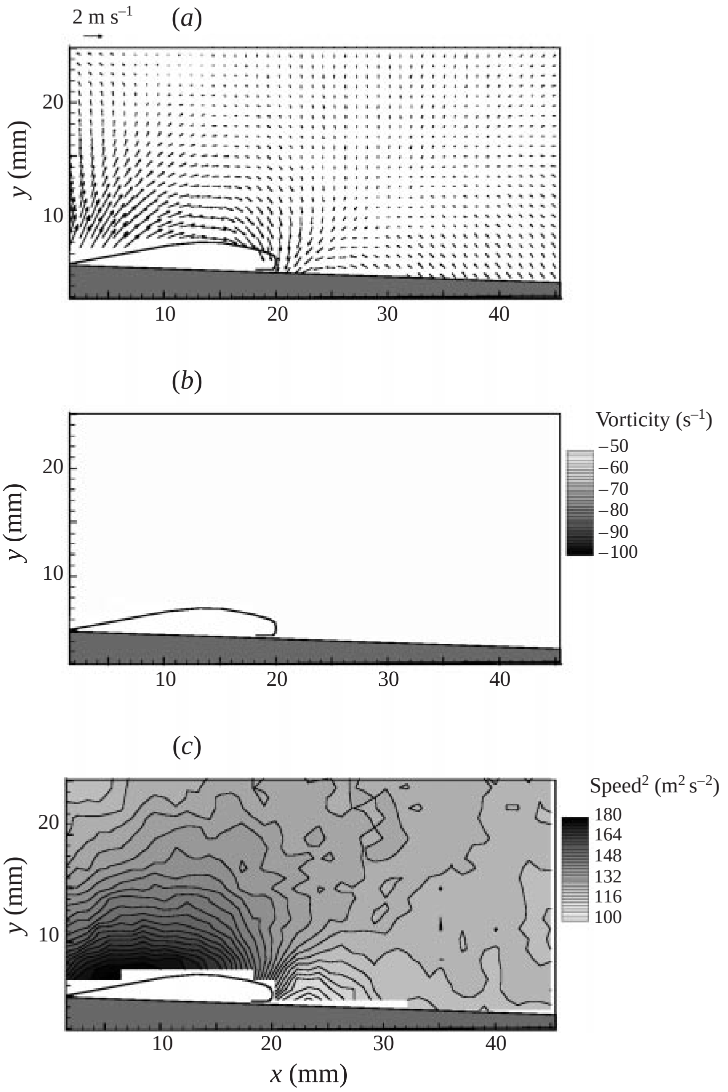

FIGURE 15. Averaged PIV velocity vector field on the three-dimensional, plano-convex hydrofoil. $\alpha = 2^\circ$, $U = 9.8\,\mathrm{m\,s^{-1}}$, $\sigma = 0.75$. (*a*) Velocity field with global mean subtracted, $U_{gm} = 11.4\,\mathrm{m\,s^{-1}}$, $V_{gm} = 1.6\,\mathrm{m\,s^{-1}}$. (*b*) Vorticity plot. (*c*) Flow speed $|\boldsymbol{u}|^2 = u^2 + v^2$. 50 images were processed.

3.4. *Flow near the cavity and in the closure region*

Figure 14 presents the phase-averaged velocity field for a series of 50 images of cavities on the three-dimensional wedge, and figure 15 presents the averaged velocity field for the swept hydrofoil ($\gamma = 30^\circ$) for $\alpha = 2^\circ$ taken at the mid-plane. Figures 14(*a*) and 15(*a*) show the velocity field with the average velocity subtracted out, and figures 14(*b*) and 15(*b*) present the corresponding averaged vorticity plot. Figures 14(*c*) and 15(*c*) show a contour plot of the square of the local average flow speed, $|\boldsymbol{u}|^2 = u^2 + v^2 + w^2$ which is related to the local pressure by $(1 - C_P) \approx |\boldsymbol{u}^2|/U_\infty^2$. The velocity component in the spanwise direction, w, was not necessarily zero, and this component was not measured. If we compared the maximum value of $|\boldsymbol{u}|^2_{streamwise} = u^2 + v^2$ with the independently measured cavitation number and the free-stream velocity, the magnitude of w can be

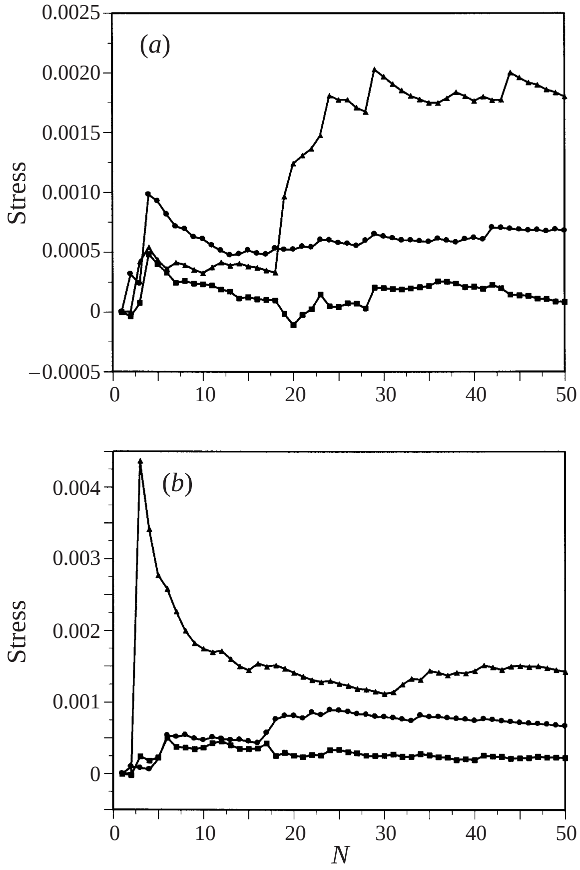

FIGURE 16. Convergence plots for the Reynolds stresses on (*a*) the three-dimensional wedge, and (*b*) convergence plots for the Reynolds stresses on the three-dimensional, plano-convex hydrofoil: ●, $\overline{(u/u_o)'(u/u_o)'}$; ▲, $\overline{(v/u_o)'(v/u_o)'}$; ■, $\overline{(u/u_o)'(v/u_o)'}$. N is the number of averaged images.

estimated since $(1+\sigma) \approx |\boldsymbol{u}|^2/U_\infty^2$ at the cavity interface. Near the maximum thickness of the cavity, $(1+\sigma)U_\infty^2 \approx 170\,\mathrm{m^2\,s^{-2}}$, and this was within about ±5% of the value measured with the PIV system. Thus, near the point of maximum cavity thickness, $w^2/(u^2+v^2) \approx 5\%$, making the maximum possible value of the spanwise component equal to approximately 20% of the streamwise component (~ 2 to $3\,\mathrm{m\,s^{-1}}$). Near the cavity closure, as the velocity decreased, the spanwise component may be the largest. Here, $|\boldsymbol{u}|^2_{streamwise} = u^2+v^2 \approx 100\,\mathrm{m^2\,s^{-2}}$ and a value of $w = 3\,\mathrm{m\,s^{-1}}$ would introduce an error of $w^2/(u^2+v^2) \approx 9\%$. It was possible that the spanwise component extended the region of low pressure farther downstream, but the general isobars around the cavity would not be significantly modified. The pressure near the cavity surface reached a minimum near the centre of the cavity, and an adverse pressure gradient was observed near the closure of the cavity.

Fluctuating components of the flow fields were also determined for the series of 50 images. The average turbulence quantities $\overline{(u/u_o)'(u/u_o)'}, \overline{(v/u_o)'(v/u_o)'}$, and $\overline{(u/u_o)'(v/u_o)'}$ never exceeded 0.5%, where u_o is a measured velocity in the interrogation region far from the cavity. The highest turbulence levels were observed very near the

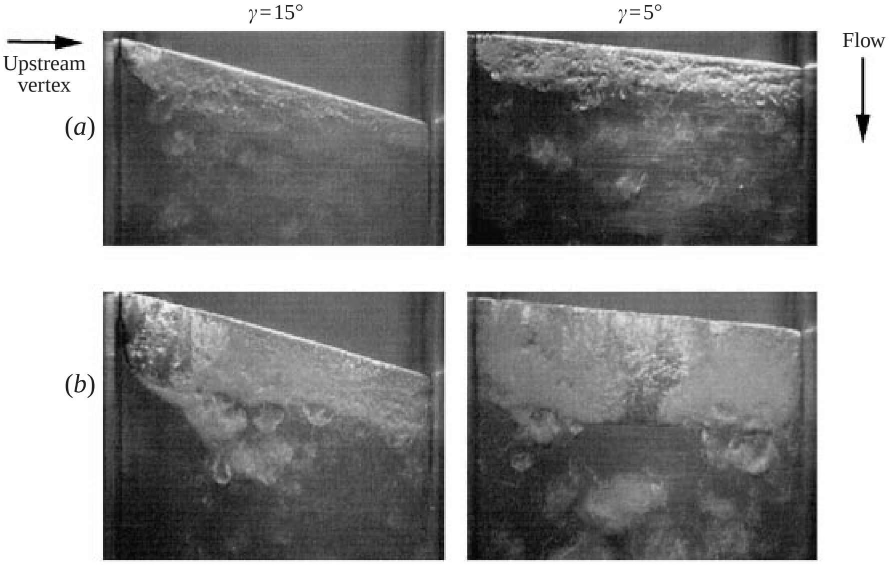

FIGURE 17. Effect of sweep angle at $\alpha = 2°$. $\gamma = 15°$: (*a*) $U = 9.2\,\mathrm{m\,s^{-1}}$, $\sigma = 0.9$; (*b*) $U = 9.7\,\mathrm{m\,s^{-1}}$, $\sigma = 0.8$. $\gamma = 5°$: (*a*) $U = 9.6\,\mathrm{m\,s^{-1}}$, $\sigma = 1.0$; (*b*) $U = 9.5\,\mathrm{m\,s^{-1}}$, $\sigma = 0.8$. Plan view.

sharply curved terminus of the cavity interface. Otherwise, the turbulence levels were less than 0.1%. The convergence plot for these averaged images are shown in figures 16(*a*) and 16(*b*). Overall, the flow remains essentially laminar and irrotational.

3.5. *Effects of hydrofoil sweep angle*

The cavitating flow on hydrofoils with $\gamma = 15°$ and $5°$ was examined to determine the effect of varying sweep. Figure 17 presents the cavity appearance on these hydrofoils for an attack angle of 2°. At the low attack angle, a clear cavity can be seen on the $\gamma = 15°$ swept hydrofoil near the upstream leading edge. A large portion of the cavity was a liquid/vapour mixture, which was similar to the open cavities on the two-dimensional plano-convex hydrofoil. At the higher attack angle, closed cavities were not observed. For the $\gamma = 5°$ hydrofoil, closed cavities were not observed for any of the test conditions. The cavities were all similar to those observed on the two-dimensional plano-convex hydrofoil of Part 1.

4. The absence of flow separation at the terminus of the cavity and the creation of re-entrant flow

It is interesting to note that the flow around the closed partial cavities remained largely irrotational and that a re-entrant closure was observed. These are the conditions that are often employed in the formulation of a potential flow solution of cavity flows. The re-entrant closure model employed in the free-streamline model represents a laminar reattachment of the cavity flow. The boundary layer over the closed cavity interface was not observed to separate from the interface. This is expected, as any vortical flow near the cavity interface will be confined to a thin boundary layer.

First, consider the boundary layer over the cavity interface. A thin boundary layer may be present upstream of the cavity detachment that could be ingested over the cavity. Yu & Ceccio (1997) measured the momentum thickness of the boundary layer upstream of the two-dimensional wedge vertex to be on the order of $\theta_D \approx 10^{-4}\,\mathrm{m}$

making $\theta_D/L_C \approx 10^{-6}$. Vorticity can also be created at a steady free surface as a result of surface curvature, where the rate of vorticity generation is proportional to the curvature of the free surface. Batchelor (1967) showed that the vorticity generation, $\Delta\omega$, at a stationary, two-dimensional free surface is given by $\Delta\omega = (2\kappa U_C)_{FS}$, where κ is the curvature of the intersection of the free surface with the plane normal to it. The curvatures of the cavities studied here are on the order of $10\,\mathrm{m}^{-1}$ except for the region of sharply increased curvature at the closed cavity closure. The free-surface boundary layer grows by diffusion and convection, and the thickness of this boundary layer near the cavity closure, δ_{FS}, can be scaled with $\delta_{FS} \approx (L_C \nu/U_C)^{1/2} \approx 10^{-5}\,\mathrm{m}$. The jump in velocity across the free-surface boundary layer is on the order of $\Delta U_C \approx \delta_{FS}\Delta\omega$. With $U_C \approx 10\,\mathrm{m\,s^{-1}}$, $\Delta U_C/U_C \approx 10^{-2}$. Therefore, it is expected that the boundary layer over the length of the cavity interface remains very thin and that the velocity gradient across the boundary layer is small.

It was experimentally observed that the liquid flow remained attached to the contour of the closed cavity, except for the region of large cavity curvature near the downstream extent of the cavity. The absence of large-scale flow separation is expected, since the shear stresses on the smooth cavity interface are negligible, and the thin boundary layer near the cavity interface would not experience an adverse pressure gradient. Recall that the cavity interface ideally represents a constant-pressure interface. Therefore, the fluid elements within the thin boundary layer on the cavity interface should not be subjected to an adverse pressure gradient in the direction normal to the cavity interface. Without any decelerating stresses, the fluid within the free-surface boundary layer will remain attached to the cavity interface. The flow only separates from the cavity at the region of high curvature near the terminus of the cavity. Consequently, the flow remains attached to the cavity interface and curves around its terminus to form a stagnation flow and re-entrant jet.

The absence of large-scale flow separation suggests that open cavities do not result from boundary layer separation at the cavity interface. Instead, as suggested in Part 1, open cavities result from premature condensation of the partial cavity. With the absence of large-scale condensation, the cavity can form a re-entrant closure. Figure 18 shows a comparison between the measured velocity magnitude around the open cavity of the two-dimensional wedge (*a*), the closed cavity on the swept wedge (*b*), and the analytical solution for the cavity flow corresponding to the conditions on the two-dimensional wedge (*c*). The analytical results are plotted with the resolution of the PIV images. For the case of the open cavity, the adverse pressure gradients occur the farthest upstream. The gradients near the surface of the closed cavity are weaker. Lastly, the pressure over the cavity interface remains constant for the analytical solution, as assumed.

5. Steady re-entrant versus unsteady re-entrant partial cavities

The closed cavities observed on the swept wedge and hydrofoil had a steady geometry and did not shed cloud cavitation. The flow around these cavities was largely laminar and irrotational. These cavities were *steady re-entrant* cavities. This flow can be compared to the cavity flow around the NACA0009 two-dimensional hydrofoil discussed in Part 1. The flow around the partial cavity on the NACA0009 hydrofoil was essentially laminar and irrotational as well, but very unsteady. However, the cavity on the NACA0009 hydrofoil shed large cloud cavitation. These were *unsteady re-entrant* cavities. These differences in observed cavity dynamics are due to differences in the re-entrant flow. In the case of the three-dimensional closed cavities

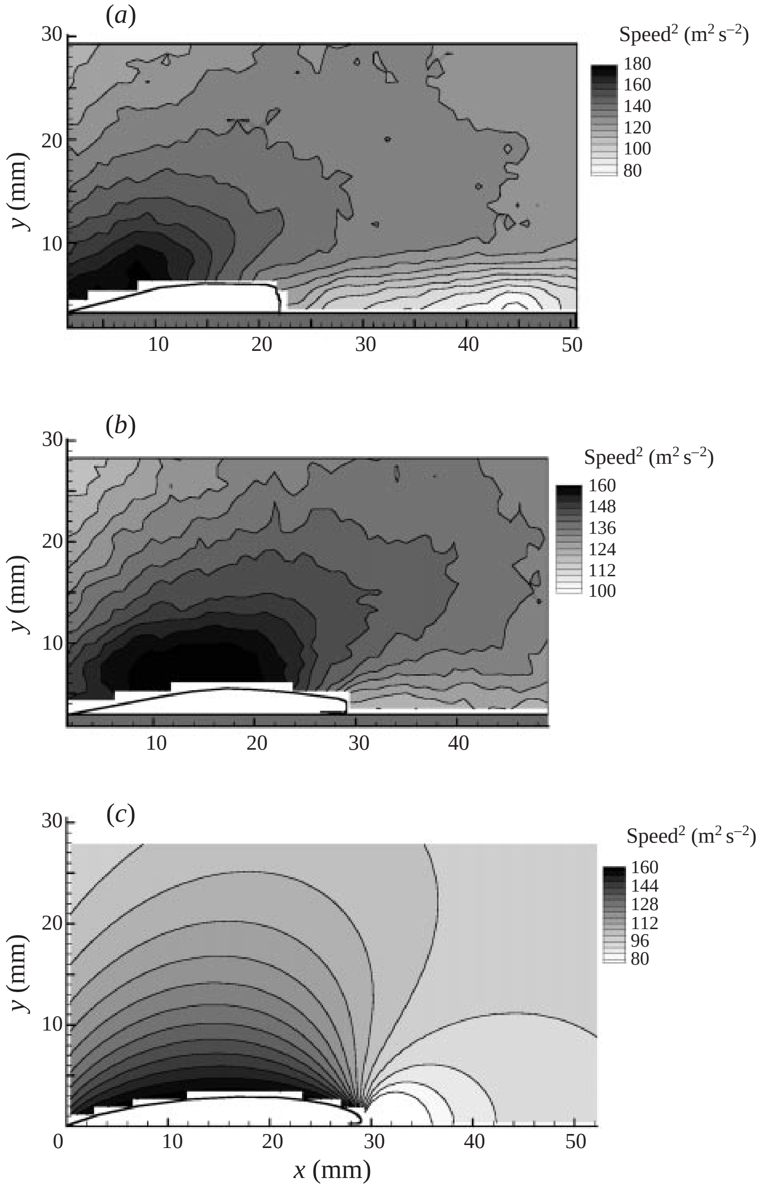

FIGURE 18. A comparison of the velocity magnitude $|\boldsymbol{u}|^2 = u^2 + v^2$ of the flow near (*a*) the open cavity on the two-dimensional wedge, $\beta = 26.5°$, $U = 8.4\,\mathrm{m\,s^{-1}}$, $\sigma = 1.9$, and (*b*) the closed cavity on the three-dimensional wedge, $\beta = 26.5°$, $\gamma = 30°$, $U = 8.4\,\mathrm{m\,s^{-1}}$, $\sigma = 1.5$. Also plotted is the analytical solution for a two-dimensional closed cavity with a profile that approximately matches that of the three-dimensional closed cavity (*c*). The analytical solution corresponds to values of $l_C = 29\,\mathrm{mm}$ and $\sigma = 1.96$. The analytical solution is plotted with the resolution of the PIV images.

on the swept test objects, the re-entrant flow moved in the spanwise direction, and a cavity with stable geometry was formed. In the case of the NACA0009 hydrofoil, the re-entrant flow was directed upstream, and its impingement on the cavity interface caused periodic shedding of cloud cavitation. Large cavitation clouds were shed via the classically described mechanism for cloud cavitation, in which a re-entrant jet flow within the cavity impinged on the cavity surface and lead to cloud break-off.

6. Conclusions

The cavity flows examined in the present study are canonical in nature, but they reveal interesting phenomena that are instructive about cavitation that forms on more complex geometries. Closed cavities were observed, and the underlying processes that resulted in these very different cavity topologies were investigated. Several conclusions can be drawn:

(i) The topology of the cavity can be significantly changed when spanwise gradients are introduced into the flow. If re-entrant flow exists in the closure of a three-dimensional partial cavity, the re-entrant flow may be redirected away from the cavity interface allowing a steady, closed cavity to form.

(ii) The cross-sectional profile of three-dimensional closed cavities was qualitatively similar to the two-dimensional profiles predicted with free-streamline theory. The flows around closed cavities were essentially irrotational and laminar.

The cavities examined in this study and in Part 1 were formed on stationary test objects. Studies of cavitation on moving test objects suggest that these dynamic cavities exhibit features of the cavity flows on steady test objects, such as the re-entrant flow in the cavity closure and the formation of cloud cavitation (see, for example, the study of cavitation on pitching hydrofoils by Shen & Peterson 1978; Hart, Brennen & Acosta 1990; and Reismann & Brennen 1996). Cavity flows on unsteady test objects can be characterized with a dimensionless time scale whereby the convection time scale, $U_\infty L$, is compared with a time scale related to the motion of the cavitating object. A reduced frequency $\omega/U_\infty L$ can be defined for a periodically moving test object of oscillating frequency ω. If $\omega/U_\infty L \ll 1$, we expect that the flow is quasi-steady and partial cavities that form will be similar to those observed on steady test objects. However, when $\omega/U_\infty L > 1$, we would no longer expect the quasi-steady assumption to apply.

The authors would like to thank Ann Tassin-Leger and Claudia Iyer for their assistance during the completion of this research. We would also like to acknowledge the substantial effort of Christopher Kubacki, Daniel Peterman, and Brian Brunzell during the processing of the experimental data. This work was supported by the Office of Naval Research, under contract N00014-96-1-0076, with Dr Edwin Rood as the technical monitor.

REFERENCES

Bark, G. 1985 Development of distortions in sheet cavitation on hydrofoils. *Proc. Jets and Cavities – Intl Symp., Miami Beach, Florida, USA*, pp. 215–225. ASME.

Bark, G. 1986 Development of violent collapses in propeller cavitation. *Proc. Intl Symp. on Cavitation and Multiphase Flow Noise, Anaheim, CA, USA*. ASME-FED, vol. 45, pp. 65–75.

Batchelor, G. K. 1967 *An Introduction to Fluid Dynamics*. Cambridge University Press.

Crimi, P. 1970 Experimental study of the effects of sweep on hydrofoil loading and cavitation. *J. Hydraul.* **4**, 3–9.

Dang, J. & Kuiper, G. 1999 Re-entrant jet modeling of partial cavity flow on three-dimensional hydrofoils. *Trans. ASME: J. Fluids Engng* **121**, 781–787.

Hart, D. P., Brennen, C. E. & Acosta, A. J. 1990 Observations of cavitation on a three-dimensional oscillating hydrofoil. *Proc. ASME Cavitation and Multiphase Flow Forum.* FED, Vol. 98 (ed. O. Furuga), pp. 49–52.

Ihara, A., Watanabe, H. & Shizukuishi, S. 1989 Experimental research of the effects of sweep on unsteady hydrofoil loadings in cavitation. *Trans. ASME: J. Fluids Engng* **111**, 263–270.

Laberteaux, K. L. & Ceccio, S. L. 2001 Partial cavity flows. Part 1. Cavities forming at the vertex of wedges. *J. Fluid Mech.* **431**, 1–41.

Lange, D. F. de 1996 Observation and modelling of cloud formation behind a sheet cavity. PhD thesis, University of Twente, The Netherlands.

Reisman, G. E. & Brennen, C. E. 1996 Pressure pulses generated by cloud cavitation. *Proc. ASME Symp. on Cavitation and Gas–Liquid Flows in Fluid Machinery and Devices*. ASME-FED, vol. 236, pp. 319–328.

Shen, Y. T. & Peterson, F. B. 1978 Unsteady cavitation on an oscillating hydrofoil. *Proc. 12th Symp. on Naval Hydrodynamics*, pp. 362–384.

Tassin, A. L., Li, C.-Y, Ceccio, S. L. & Bernal, L. P. 1995 Velocity field measurements of cavitating flows. *Exps Fluids* **20**, 125–130.

Thwaites, B. 1960 *Incompressible Aerodynamics*. Dover.

Yu, P. W. & Ceccio, S. L. 1997 Diffusion induced bubble populations downstream of a partial cavity. *Trans. ASME: J. Fluids Engng* **119**, 782–787.